*Materials Research*. 2019; 22(4): e20190302
DOI: http://dx.doi.org/10.1590/1980-5373-MR-2019-0302

# Influence of the Gas Pressure of Plasma Nitriding on the Structural, Mechanical and Tribological Surface Properties of AISI 316L

***Marcelo Campos*[a]*, *Solange de Souza*[b], *João Paulo Davim*[c], *Sylvio Dionysio de Souza*[b], *Maristela Olzon-Dionysio*[b]**

[a]*Faculdade de Ciências e Engenharia, Universidade Estadual Paulista (UNESP), Tupã, SP, Brasil*
[b]*Universidade Federal dos Vales do Jequitinhonha e Mucuri (UFVJM), Diamantina, MG, Brasil*
[c]*Departamento de Engenharia Mecânica, Universidade de Aveiro (UA), 3810-193, Aveiro, Portugal*

Received: April 22, 2019; Accepted: May 19, 2019

In this paper, the influence of gas nitriding (80% $H_2$-20% $N_2$) pressure (between 3 and 7 Torr) on the modification of surface properties of AISI 316L stainless steel is examined. The structural, mechanical, tribological and electrochemical properties of the layer produced in disk samples were studied. The samples' characteristics were determined by scanning electron microscopy, X-ray diffraction, electrochemical potential curves, microhardness, roughness and wear tests. When pressure increases, the microhardness, elasticity and thickness also increase. The maximum thickness of the nitrided layer was 6.4 μm, the hardness reached 2200 $HV_{0.0036}$ and the mass loss decreased until 1% relatively to the unnitrided sample. The X-ray diffractograms showed the presence of the expanded austenite in all the samples. The correlation between these diffractograms and the corrosion results corroborate to the most recent previous conclusions of our systematic study, which evince the interconnection between the improvement of the corrosion resistance and the presence of nitrides on the top of the nitrided layer. More significant presence of such nitrides was observed for the sample nitrided at 6 Torr, whose corrosion performance was better than for the other samples. This pressure seems to be the most indicated to improve the properties under study. Moreover, the results verified not only that the sample geometry is an important factor for enhancing these properties but also that the border effect, which causes the rings on the disk border, depends on the pressure, but not on temperature or time from the plasma nitriding process.

**Keywords:** *AISI 316L stainless steel, Plasma nitriding, Gas nitriding pressure, Tribological and Mechanical properties, Synchrotron Diffraction.*

## 1. Introduction

As stainless steels ASTM F138 and AISI 316L are widely used in many areas, such as chemical and petrochemical processing, aerospace and automotive industries, as well as in biomedical engineering, as an implant material, studies on these materials have received great attention [1-4]. The important properties in this context are high hardness, wear resistance and also corrosion resistance, which can be improved by plasma nitriding. For nitriding temperatures up to 400 ºC, a nitrided layer of some micrometers is formed. It is composed by the *composite layer*, which consists of iron and chromium nitrides and concentrates on the surface, as well as the nitrogen *diffusion layer*, located in the inner region, known as expanded austenite or $\gamma_N$.

When compared to the correspondent austenite ($\gamma$) peaks, the $\gamma_N$ presents broad diffraction lines, which is due to the gradient of nitrogen, residual stresses and a possible defect structure of the nitrided layers [5,6]. The structure of $\gamma_N$ is still a matter of debate and besides not yet having been completely clarified [6-10], it also seems to depend on the nitrogen content. Fewell and Priest [8] tested a total of ten plausible candidate structures in order to propose a structure for this phase, among them the tetragonal, monoclinic and triclinic, obtaining the best description of their data from the last one using a sample whose nitrogen content was relatively low. If it increases, some effects such as high density of stacking faults and high compressive residual stress [9,10] cannot be ignored. On the other hand, the $\gamma_N$ lines are commonly in the same region as the formed nitrides, causing an intrinsic difficulty in detecting them in the diffraction patterns.

The nitrided layer properties are directly related to the phases produced during the treatment, which, in turn, are strongly dependent on the parameters used on plasma nitriding (gas mixture, pressure, temperature and time) [1,11,12].

This paper is part of a larger study on the plasma nitriding process applied to austenite stainless steel. Our main objective is to find the best combination of the plasma nitriding parameters to optimize the properties of the nitrided layer. Our previous studies, using 80 % $H_2$-20 % $N_2$ gas, investigated the influence of temperature and time, indicating the best combination: 4h, 400 ºC [13-15]. This research has shown that

*e-mail: marcelo.campos28@unesp.br

nitrided layer properties depend much more on pressure than on temperature or time. Thus, this paper investigates the influence of pressure on some properties of the plasma nitrided layers using 80% $H_2$-20% $N_2$, 4h, 400 ºC, under 3, 4, 5, 6 and 7 Torr pressure. Results of the nitrided layer thickness, surface roughness, hardness, wear and corrosion tests and X-ray diffraction patterns are discussed.

## 2. Material and Methods

### *2.1 Samples*

In this study, AISI 316L stainless steel produced by Villares Metals was used for the samples (disk diameter: 19.70 ± 0.05 mm, thickness: 2.00 ± 0.02 mm). Its chemical composition (only elements with wt.% > 0.10) is: 16.1 ± 0.2 Cr, 10.1 ± 0.1 Ni, 2.1 ± 0.1 Mo, 1.80 ± 0.02 Mn, 0.37 ± 0.05 Si, 0.31 ± 0.04 Cu, 0.180 ± 0.004 W, 0.13 ± 0.01 Co, balance Fe. The samples were plasma nitrided using 80 % $H_2$-20 % $N_2$, at 400 ºC, for 4h, at different pressures, between 3 and 7 Torr (3, 4, 5, 6, 7), called P3 until P7. Details of nitriding have been given previously [16].

### *2.2 Scanning electron microscopy*

A section of the samples was observed using a JEOL scanning electron microscope, JSM - 5800 LV model in order to measure the depth of the nitrided layer.

### *2.3 Hardness*

The surface hardness was measured using a Fischerscope H100V microhardness tester with a Vickers indenter at a load of 35 mN (~3.6 gf). The hardness was measured along the diameter, equally spaced at 0.25 mm. Due to the low load used, a special computational routine, which was developed for treating similar data, was used in the data treatment [17].

### *2.4 Roughness*

The surface roughness was measured using a Hommel Werke T1000 rugosimeter. The roughness was measured along the radius.

### *2.5 Wear tests*

Dry sliding tests were carried out using a Pin on a Disk Plint TE67/HT tribometer with a normal constant load of 100 N. The Pins were the samples and the disk was AISI 1045 Steel, set at 41.5 rpm and 1 km of the sliding distance.

### *2.6 Corrosion*

Corrosion performance characterizations in a 3 % NaCl aerated electrolytic solution were carried out for the nitrided samples, and also an unnitrided one, to be used as a reference. Electrochemical experiments were performed at room temperature in a conventional Pyrex cell. Samples were used as working electrodes and a platinum sheet as the counter electrode. The potentials were referred to the saturated calomel electrode (SCE) in a KCl solution. Potentiodynamic anodic polarization curves were investigated using a PGSTAT30 Potentiostat/Galvanostat from Autolab (Eco Chemie, Netherlands). The scanning potential was in the range between the cathodic and anodic potential, with a scan rate of 1.0 mV. $s^{-1}$.

### *2.7 X-ray diffraction*

The phases formed in the nitrided samples were characterized by X-ray diffraction (XRD), performed at the Brazilian Synchrotron Light Laboratory (LNLS), using synchrotron radiation for two measurements. The conditions were: λ=1.9074 Å or E=6.500 keV, θ-2θ geometry, ranging from 47º ≤ 2θ ≤ 135º and scan step of 0.2° for the first one. For the second, λ=1.6530 Å or E=7.500 keV, incident angle fixed $\theta = 2°$, ranging from 47º ≤ 2θ ≤ 66º and scan step of 0.04°, named Glancing Angle X-Ray Diffraction (GAXRD).

In order to compare this sample set with the previous[18] from our systematic study, these XRD data were analyzed assuming the same special triclinic symmetry [8,13] for this phase, which presents a slight angular distortion (η) from the FCC austenitic substrate structure and calculating the values for nitrogen content ($C_N$) through the Picard's equation[19]:

$$a_{\gamma N} = a_{\gamma} + \alpha\, C_N$$

where $a_{\gamma N}$ and $a_{\gamma}$ are the lattice parameter for expanded austenite $\gamma_N$ and austenite $\gamma$, and α is a constant. Instead of 0.00861 Å/at.% N [20], which was previously used for this constant, the value 0.013 Å/at.% N [21] was used, because it seems more appropriate for the present case.

## 3. Results

### *3.1 Rings on nitrided disks (Edge effect)*

Fig 1(a) shows the picture of the P6 sample, where an external ring (in a light colour) and a very thin region (in a dark colour) can be seen, which takes place because of the edge effect [16]. These regions are called the border and intermediate. Going towards the center, there is the third one: the central region. For better precision, the ring extension (RE), which is indicated in Fig 1(a) was measured using optical microscopy images of this region, which are shown in Fig 1(b) for P3 and P7. Fig 1(c) exhibits the RE results for all samples.

### *3.2 Nitrided layer thickness*

Figs 2(a), (b) and (c) show the SEM micrographs for different regions (border, intermediate and central regions) for the P3 sample. Fig 2(d) shows the thickness (**t**) for these regions for all the samples.

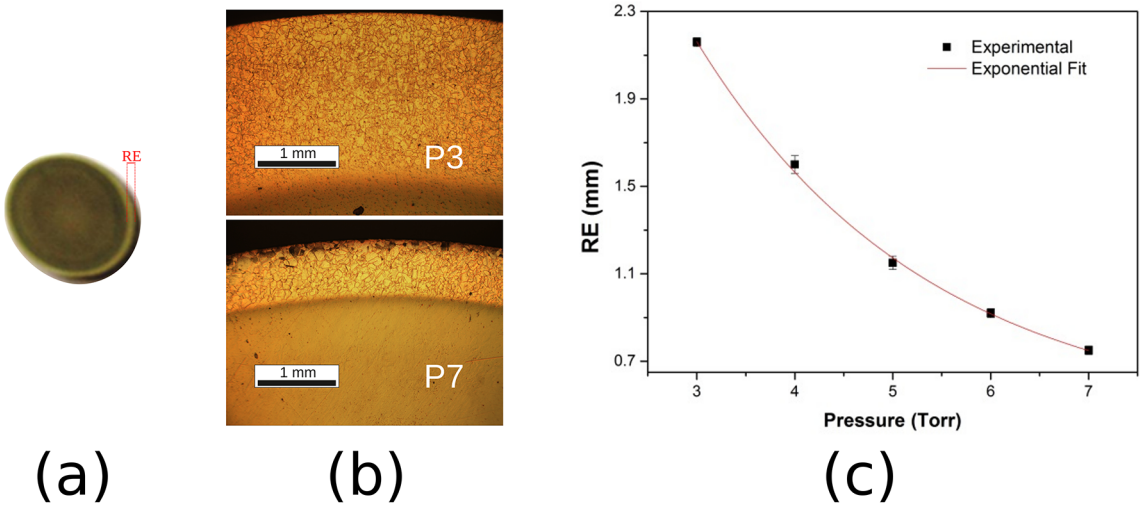


**Figure 1.** (a) Visual aspect of ring formed on the border of the P6 sample; (b) Optical microscopy image of ring for P3 and P7; (c) Extension of ring as a function of the nitriding pressure.

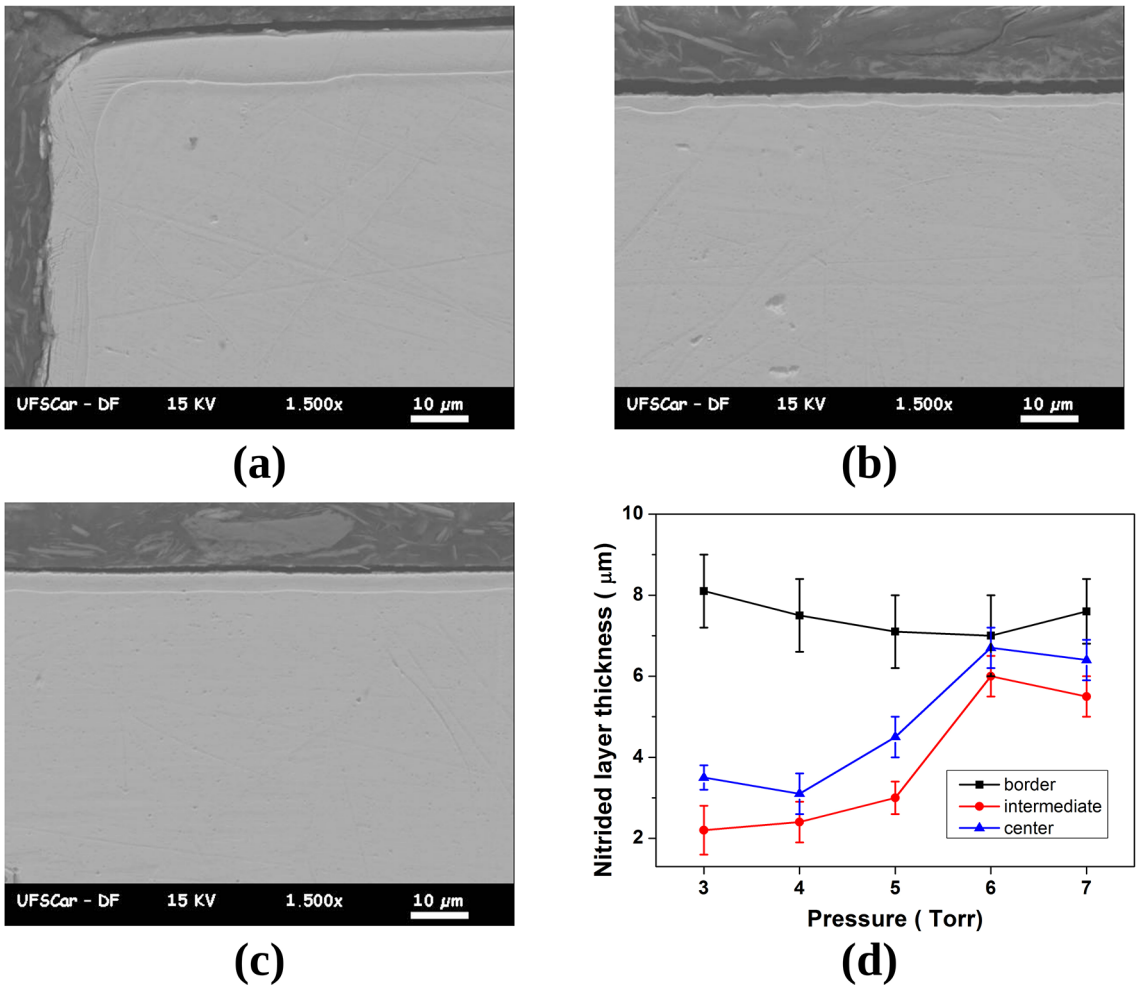


**Figure 2.** SEM micrographs of the P3 sample, nitrided at 3 Torr, for different regions: (a) border; (b) intermediate; (c) central; (d) thickness measurements for different regions as a function of the nitriding pressure.

### *3.3 Hardness and elasticity*

Fig 3 (a) shows the hardness for all the samples, for the three regions (border, intermediate and central). To see the validity of these results, it is important to avoid the substrate influence (H=250±14 $HV_{0.036}$) in hardness measurements. Thus, Fig 3 (b) presents hardness values as a function of the ratio between penetration depth (p) of the Vickers indenter and nitrided layer thickness (t). The value of 1/10 is used as a reference [17], which is shown in Fig 3(b).

Fig 4 shows the elastic modulus for the border and central regions.

### *3.4 Roughness and wear tests*

Table 1 shows the results for wear and roughness tests.

### *3.5 Corrosion*

Is is important to mention that these tests were carried out in the central region, in order to avoid the border region, where there is $Cr_2N$ [16]. The potentiodynamic anodic polarization curves for all the samples are presented in Fig 5. The curve for the unnitrided sample is included for the sake of comparison.

### *3.6 XRD*

The Synchrotron XRD patterns, for the θ-2θ geometry are shown in Fig 6 (a) and (b). The vertical bars show the fcc austenite (hkl) peak positions, which are practically the same for $\gamma_N$ formed on P3 because of its very low $C_N$.

The Synchrotron GAXRD patterns, which were collected for the (111) and (200) reflections, at the incident angle $\theta$ = 2°, are shown in Fig 7.

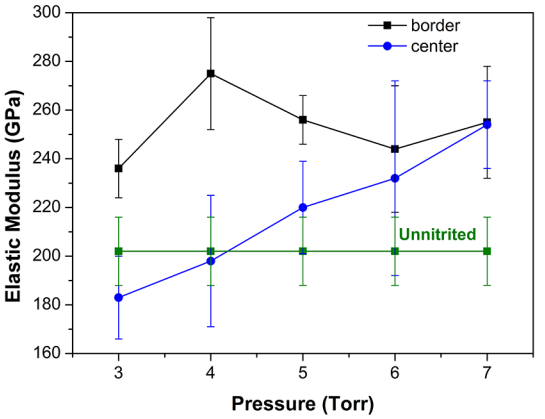


**Figure 4.** Elasticity values on border and central regions as a function of the nitriding pressure.

## 4. Discussion

### *4.1 Edge effect and nitrided layer thickness*

Before discussing the present results for the external rings formed on the nitrided disks, it is interesting to comment the results of ring extension (RE) from our previous study [22], for the samples nitrided at different times (3, 4, and 5h) and temperatures (T= 350, 400 and 450 °C). These results have not been published and are shown in Table 2.

Table 2 shows that RE does not depend on temperature (between 350 and 450 °C) or on time (between 3 and 5h). On the other hand, Fig 1 (c) shows that the RE decreases exponentially with nitriding pressure.

Regarding Fig 2 (d), in the border region, the thickness (t ≈ 7.4 ± 0.3 μm) is statistically independent on nitriding

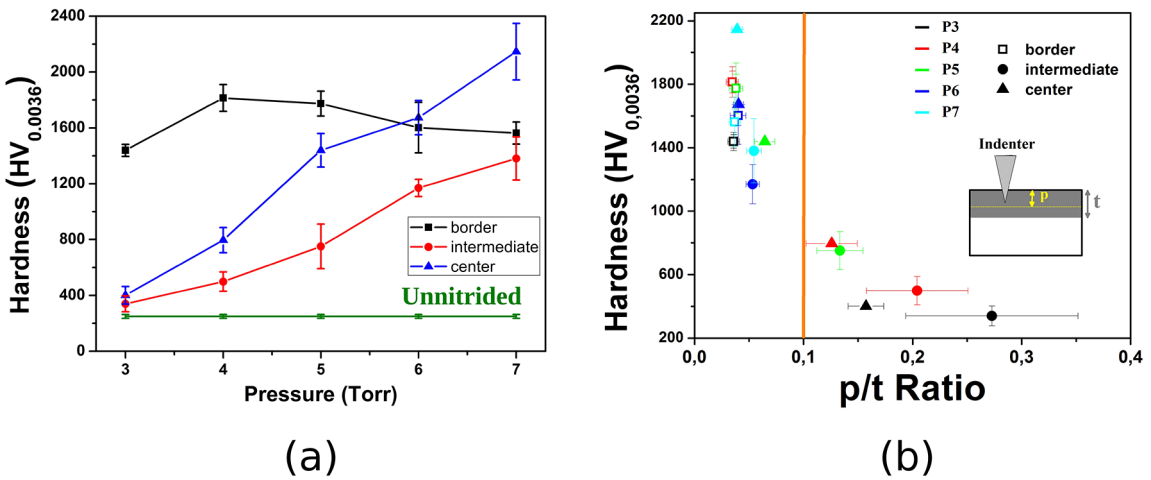


**Figure 3.** (a) Hardness values on border, intermediate and central regions as a function of the nitriding pressure; (b) Hardness values as a function of the ratio between penetration depth (p) and nitrided layer thickness for the different regions of the nitrided samples.

**Table 1.** Measurements of surface roughness, friction coefficient and mass loss during wear test.

| Pressure (Torr) | Friction Coefficient | Mass Loss (mg) | Roughness (μm) |
|---|---|---|---|
| Unnitrided | 0.53±0.01 | 558.3±0.5 | 0.003 ±0.003 |
| 3 | 0.67±0.03 | 121.1±0.5 | 0.035±0.007 |
| 4 | 0.60±0.02 | 193.6±0.5 | 0.04±0.01 |
| 5 | 0.78±0.02 | 16.2±0.4 | 0.05±0.01 |
| 6 | 0.70±0.02 | 6.1±0.3 | 0.093±0.004 |
| 7 | 0.57±0.01 | 7.8±0.3 | 0.06±0.02 |

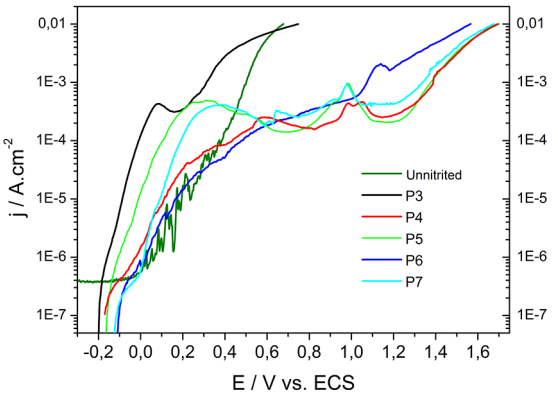


**Figure 5.** Potentiodynamic anodic polarization curves for samples nitrided at different pressures and unnitrided; in 3% NaCl aerated electrolytic solution.

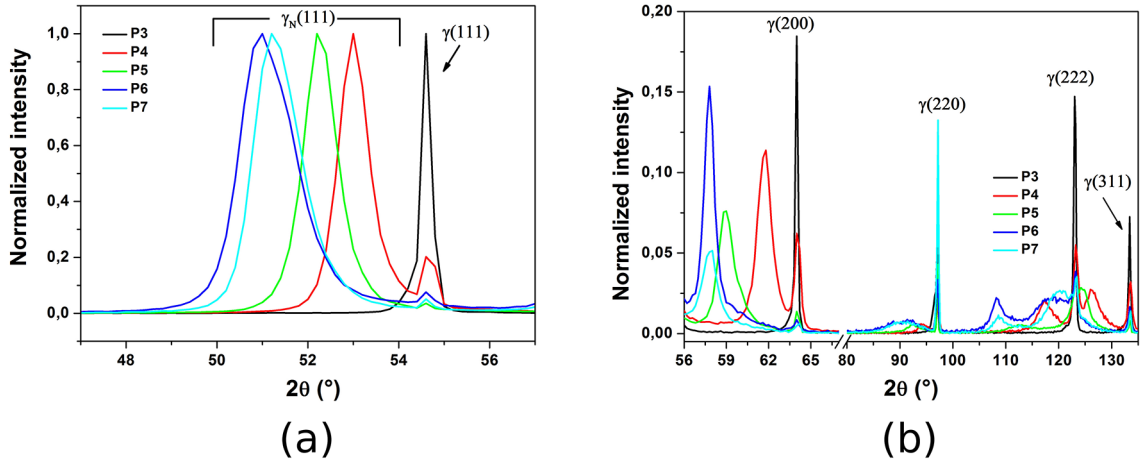


**Figure 6.** XRD patterns, at the θ-2θ geometry, using E=6.5 keV, of the reflections: (a) (111); (b) (200), (220), (222) and (311), for the samples nitrided at different pressures.

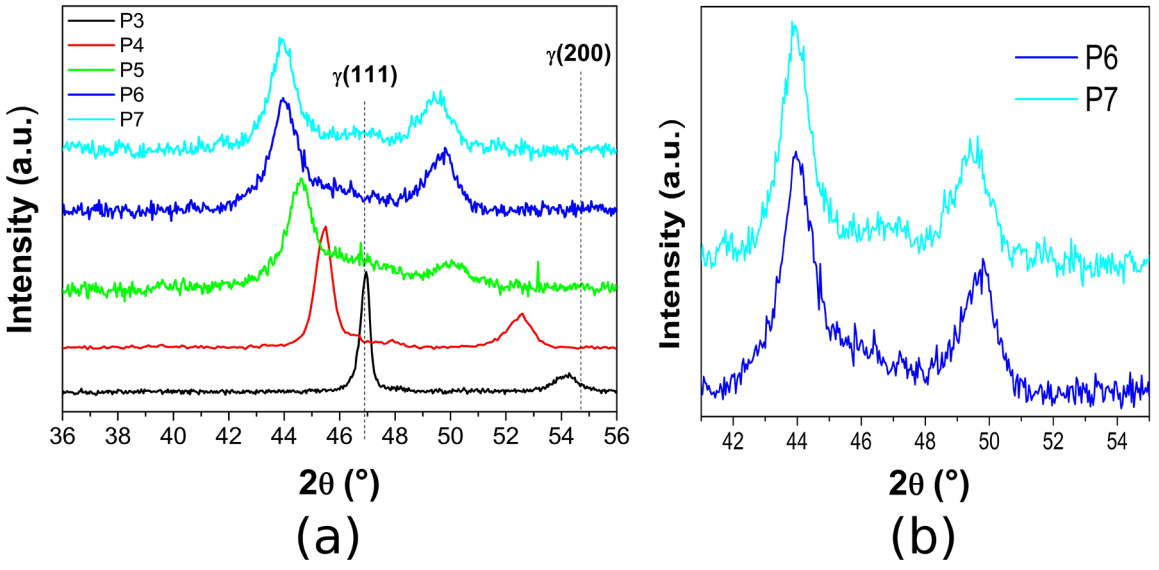


**Figure 7.** GAXRD patterns (θ=2°) of the reflections (111) and (200) (a) for all the nitrided samples, (b) zoomed, for 6 and 7 Torr.

**Table 2.** Ring Extension (RE) results for samples nitrided under 6 Torr, at 350, 400 and 450 °C, for 3, 4 or 5h.

| Ring Extension (RE) ± 0.05 mm | | | |
|---|---|---|---|
| Time (h) | Temperature (°C) | | |
| | 350 °C | 400 °C | 450 °C |
| 3 | 0.68 | 0.74 | 0.72 |
| 4 | 0.70 | 0.65 * | 0.71 |
| 5 | 0.71 | 0.67 | 0.76 |

(* the same conditions used in this paper).

pressure. In the central and intermediate regions, it increases up to 6 Torr and then it stabilizes. The thickness for the intermediate region is smaller than for the center region, except for P6, whose thickness is practically uniform.

Borgioli et al.[12] investigated the influence of pressure on plasma nitriding of AISI 316L and their Table 2 shows that thickness decreases when the pressure increases, which is not compatible with the present results. Therefore, not only is the gas composition a very important parameter in this treatment, but also the pretreatment that they used.

It is interesting to compare the present results for the ring extension (RE) and nitrided layer thickness (t) in the central region with our previous results for samples with a different diameter (D) and height (h), which were nitrided in the same conditions[16,23] (Table 3).

Table 3 shows that when the sample height increases, t and RE decrease; on the other hand, if the sample diameter increases, t increases and RE remains constant. Therefore, the sample geometry is also an important factor for these properties of the nitrided layer, most likely because of the temperature gradient [24,25].

It is interesting to comment about the much higher thickness (16.5 μm) produced by De Las Heras et al [1] for 4.9 Torr (20% $N_2$- 80% $H_2$), using D=25.14 mm and h=10.00 mm. Although D should contribute to this increase, h should go in the opposite direction more significantly. However, in addition to using a time of 20h, these authors pre-treated the sample.

## *4.2 Mechanical and tribological properties*

Regarding the ***hardness***, Fig 3(a) shows that in the *border region*, P4, P5 and P6 hardness is statistically equal, with the highest values. The P3 (P4) sample shows the lowest (highest) hardness value, but the difference of the mean value (1638 $HV_{0.036}$) is only ~12 %, for both of them. This difference is insignificant, compared to the hardness value for other regions, possibly because of the determinant contribution of $Cr_2N$ in this region [16], whose hardness value is higher than 1479 HV[26,27]. The *intermediate region* presents a smaller value than the central region for all the samples. For both regions, intermediate and central, the hardness increases when the pressure increases. Fig 3(a) also shows that the center of the P5 sample presents H= 1400$HV_{0.0036}$, which corresponds to the accepted value for the $\gamma_N$ phase [28], probably because the 5 Torr pressure is enough to produce the nitriding condition for the nitrogen saturation point of the $\gamma_N$ phase[29]. Concerning P≥6 Torr, while for the P6 sample, the central and the border regions present the same hardness, the P7 central region presents a greater value than the border, which is unusually high. However, R. Wei et al. [30] also found it near 2000 HV, when N was implanted at low energy and high current densities on AISI 304. According to the authors, this process is similar to plasma nitriding; regarding the current results, certainly 7 Torr produces a higher current density than P≤ 6 Torr. Moreover, the present result for the P6 central region hardness (H= 167 (±12) x10 $HV_{0.036}$) is consistent with the previous value [23] measured for the samples nitrided at 6 Torr, 400 ºC, 3 and 5h (H=172 (±17) x10 $HV_{0.036}$ ). Finally, Fig 3(b) shows that not only for P3 and P4, but also for P5 in the intermediate region there is some substrate contribution to the hardness, because their thicknesses are not thick enough to measure the real hardness[23]. It is worth observing that not only the nitrided layer thickness (Fig 2) but also the hardness (Fig 3a) of the P6 sample are practically uniform.

Concerning ***elasticity***, the elastic modulus for the unnitrided sample is 202±14 GPa. For the border region, the mean value is 253 ± 9 GPa, which agrees with 249 GPa, a value accepted for the Cr nitrides [27], while Fig 4 shows that in the central region it increases when the pressure increases.

Regarding the ***wear resistance***, Table 1 shows that the loss mass decreases drastically for P=5 Torr, which reinforces the hardness result, which indicated the high probability of the nitrogen saturation for this sample. Table 1 also shows that P6 presents the maximum and the minimum values for the roughness and loss mass, respectively; the latter being

**Table 3.** Nitrided layer thickness (t) and ring extension (RE) for samples with different height (h) and diameter (D), for P= 4 and 6 Torr.

| | | This Work | | Previous Result for 4 Torr [4] | | | | For 6 Torr [12] | |
|---|---|---|---|---|---|---|---|---|---|
| **Sample (mm)** | **h** | 2.00 ± 0.02 | | 3.90 ± 0.05 | | 3.90 ± 0.05 | | 3.85 ± 0.05 | |
| | **D** | 20.14 ± 0.02 | | 19.70 ± 0.05 | | 31.60 ± 0.05 | | 19.70 ± 0.05 | |
| **Nitrided layer:** | | t (μm) | RE (mm) | t (μm) | RE (mm) | t (μm) | RE (mm) | t (μm) | RE (mm) |
| **Pressure (Torr)** | **4** | 3.1 ± 0.5 | 1.60 ± 0.04 | 1.5 ± 0.1 | 1.31 ± 0.06 | 2.3 ± 0.2 | 1.33 ± 0.05 | -- | -- |
| | **6** | 6.7 ± 0.5 | 0.92 ± 0.02 | -- | -- | -- | -- | 3.9 ± 0.4 | 0.65 ± 0.05 |

only 1.1 % from the loss mass for the unnitrided sample, which represents a very high improvement for this property.

### *4.3 Corrosion*

Regarding the potentiodynamic anodic polarization curves, in Fig 5, it can be said that the unnitrided sample presents a higher anodic dissolution current compared to all the others. This is evidence that the nitrided layer plays a protective role when subjected to an environment of chloride ions. Nonetheless, between ~0.0 and ~ 0.25 V, an oscillating behavior is observed, which is typical of metal in chloride solutions [31]. From then onwards, the current rises significantly due to a high metal dissolution rate. Table 4 presents the corrosion potential for all the samples. The corrosion potential of the unnitrided sample (-0.40V) is lower than that of all nitrided samples, indicating that plasma nitriding improves the corrosion resistance of the treated samples.

The maximum corrosion potential is observed for P6, ~ -0.12 V, which is similar to that of the sample nitrided at the same conditions [13].

Moreover, Fig 5 shows that the current density for the P6 sample is significantly lower than for the others, which indicates that ***for the present pressure interval, P=6 Torr produces the best corrosion resistance.***

It is interesting to compare in Fig 8, the P6 curve with the curve of the previous thinner nitrided layer (thicker sample in the Table3, penultimate column), which was nitrided in the same conditions[13]. It can be said that the corrosion resistance is still better for the thicker sample.

Therefore, from the viewpoint of corrosion resistance, this finding suggests that the thicker sample is more interesting for plasma nitriding. As the nitride formation on the top plays an important role in the corrosion resistance[13], it seems that the ***thinner nitrided layer*** of the thicker sample exhibits more nitrides on the top. Indeed, it was confirmed in the Mössbauer spectra, which showed ~ 86 % for magnetic contribution, which is mainly due to the nitrides[13], compared to 70% for the P6 sample [Olzon-Dionysio, D., personal communication, March 15, 2019].

### *4.4 DRX*

With respect to Fig 6 and 7, as the penetration depth of the synchrotron radiation [18] is greater than the thickness for all of the samples, the austenite peaks are present in all of the XRD patterns in Fig 6, but not in Fig 7, where the measurement depth was 0.63 μm, which is smaller than the thickness for all the samples. All the nitrided samples show the expanded austenite peaks, which are broader and shifted to lower diffraction angles, when compared to the correspondent austenite peaks.

The other possible phases produced in the nitriding process are the iron nitrides: ε($Fe_{2-3}N$), α´´($Fe_{16}N_2$), ξ (Fe2N) and γ'($Fe_4N$), besides the chromium nitrides CrN or $Cr_2N$. The positions of their more significant peaks are shown in Tables 5 and 6. The ε has various XRD code numbers [32-35], the another nitrides, the CRYSTMET codes are respectively: AL2472 [36], 493519 [37], 100932 [32], 493518 [37] and 510877 [38].

As can be seen, their positions are close to the two predominant phases: γ and $\gamma_N$ peaks. The enlargement of the $\gamma_N$ peaks further complicates the interpretation of these diffractograms. Therefore, for a preliminary analysis, as is our intention here, it is almost impossible to discuss the presence of these nitrides in the samples through these X-ray diffractograms. If a more realistic analysis is required,

**Table 4.** Potential corrosion for all the samples.

| Sample | Unnitrided | P3 | P4 | P5 | P6 | P7 |
|---|---|---|---|---|---|---|
| Corrosion Potential (V) | -0.40 | -0.20 | -0.19 | -0.18 | -0.12 | -0.14 |

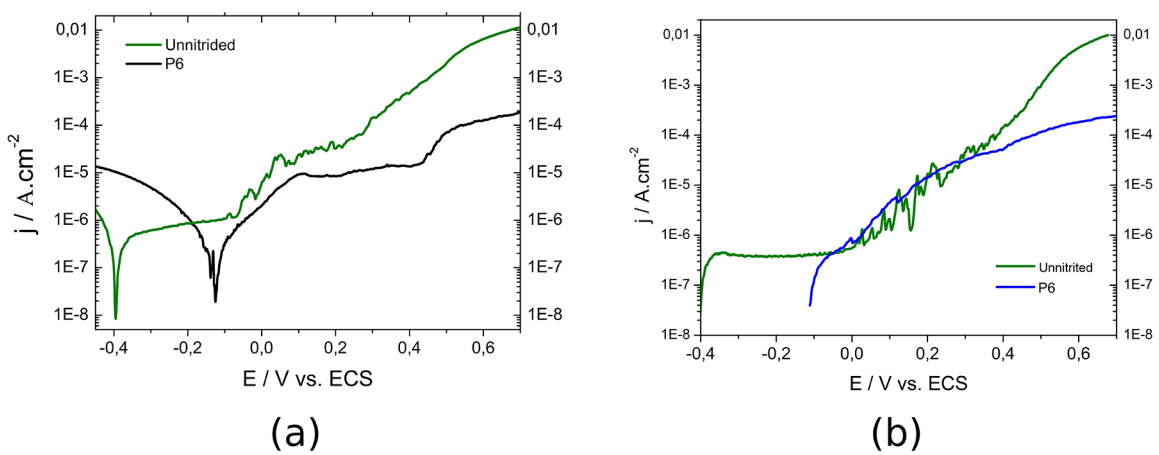


**Figure 8.** Potentiodynamic anodic polarization curves for samples nitrided at 6 Torr, showing different height (a) height =3.85 mm (b) height = 2.00 mm.

**Table 5.** Positions (°) of diffracted angles for iron nitrides.

| Phases | | γ′ ($Fe_4N$) | | | | ε ($Fe_{2-3}N$) | α′′ ($Fe_{16}N2$) | | | ξ ($Fe_2N$) | | α (Fe) |
|---|---|---|---|---|---|---|---|---|---|---|---|---|
| Relative Intensity (%) | | 100 | 58 | 33 | 31 | 100 | 100 | 51 | 30 | 50 | 100 | 100 |
| E (keV) | 6.5 | 51.7 | 60.4 | 90.7 | 113.1 | 54.9 | 53.5 | 55.3 | 51.1 | 53.6 | 53.8 | 56.1 |
| | 7.5 | 44.4 | 51.7 | 76.2 | 92.7 | 47.2 | 46.0 | 48.3 | 43.9 | 46.0 | 46.1 | 48.1 |

**Table 6.** Positions of diffracted angles for chromium nitrides.

| Phases | | $Cr_2N$ | | CrN | |
|---|---|---|---|---|---|
| Relative Intensity (%) | | 100 | 79 | 100 | 54 |
| E (keV) | 6.5 | 53.6 | 47.0 | 54.9 | 81.4 |
| | 7.5 | 46.0 | 40.5 | 47.2 | 68.9 |

the decomposition of the $\gamma_N$ peaks in subpeaks, in order to consider the nitrogen content ($C_N$) gradient across the nitrided layer is necessary and consequently the nitrides are detected [18]. Despite its limitations, this preliminary DRX data treatment can provide us with consistent information to interpret minimally the corrosion results, which indicated the P6 sample as the most resistant to corrosion.

As was said before, in order to compare the present results with the previous one, the DRX data (Fig 6) were analyzed in the same way[18], although this treatment presents major limitations, which are discussed below. The results for distortion of the triclinic structure (η) and the nitrogen content $C_N$ are shown in Table 7.

The major shortcoming of this analysis is the choice of the triclinic structure, which seems to be too simplified for such a complex system as the expanded austenite, as discussed before. Moreover, the use of α = 0.00861 Å/at.% N, which was used before for the Vegard's law to estimate the average $C_N$ may be inappropriate to extrapolate for a high concentration based on a linear correlation between the lattice parameter and atomic concentration [39]. It is used here only for the θ-2θ geometry, for the comparison within the systematic study.

Because of these failures, the calculated values for $C_N$ from Table 7 represent a rough estimate; notedly for α= 0.00861 Å/at.% N; which certainly are higher than the true values, since they are often above the expected maximum value, which is 38% [40].

In spite of this imprecision, if the whole sample set is considered, these results present some consistency. Comparing the results for both geometries, the GAXRD results for P3, P4, P5 and P7 show higher values for the distortion than for DRX, which is expected because usually more nitrogen is on the top, as can be seen for P3, P4 and P5. Regarding the P6 sample, it shows a different behavior because both of them (distortion and $C_N$) decrease for GAXRD, which happens due to the greater quantity of nitrides on the top. This can be verified in Fig 7(b), where the GAXRD pattern for P6 presents a relatively more significant slope than for P7 due to the presence of the α′′, ε and ξ nitrides, whose mean reflections are between 45° and 48°, which means that the presence of nitride on the P6 is more expressive than for P7. This result justifies the best corrosion protection for this sample[13].

Still for the sample P6, it is interesting to compare the present results for $C_N$ (corresponding to α =0.00861 Å/at.% N) calculated for the θ- 2θ geometry with the previous one for the thicker sample [18]. In the preceding case, the decomposition of the $\gamma_N$ peaks in subpeaks was used in order to consider the nitrogen gradient profile and the results were between 1.1 and 3.1° for distortion and between 12±3 and 35±3 for $C_N$. The corresponding mean values in Table 7 are 3.55 and 42.0±0.8, due to the less quantity of nitrides in the present thinner sample, which is consistent with the previous discussion about Fig 8.

**Table 7.** Nitrogen content ($C_N$) and the triclinic angular distortion (η)[8], calculated for $\gamma_N$ phase.

| Sample | | | P3 | P4 | P5 | P6 | P7 |
|---|---|---|---|---|---|---|---|
| 6,5 keV (*θ-2θ)* | η(±0.09)º | | < 0.04 | 0.38 | 3.90 | 3.55 | 3.61 |
| | $C_N$(±0.8) at % | α = 0.00861 Å/at.% N | < 3.0 | 13.9 | 34.5 | 42.0 | 42.5 |
| | | α =0.013 Å/ at.% N | <2.0 | 9.2 | 22.8 | 27.8 | 28.1 |
| 7,5 keV*θ=2º* | η(±0.09)º | | 0.98 | 0.90 | 4.29 | 3.45 | 3.89 |
| | $C_N$(±0.8) at % | α =0.013 Å/ at.% N | 2.1 | 10.3 | 24.3 | 26 | 27.6 |

## 5. Conclusion

To investigate the influence of pressure on some properties of the plasma nitrided layers, using 80% $H_2$-20% $N_2$, 4h, 400 ºC, five different values were used: 3,4,5,6 and 7 Torr. All the results are summarized as follows:

1. If the pressure increases, not only the nitrided layer thickness, but also the hardness and elasticity increase. Moreover, the loss mass decreases drastically, reaching 1% for P≥6 Torr. Besides this remarkable property, not only the nitrided layer thickness but also the hardness of the P6 sample are practically uniform along the disk diameter. Moreover, this sample shows the biggest roughness and the best corrosion resistance, presenting not only the maximum corrosion potential but also lower current density than for the other samples.
2. The X-ray diffractograms, collected at both geometries (θ-2θ and GAXRD), indicated the expanded austenite peaks for all the samples. The GAXRD can show more significant presence of nitrides for the P6 sample, which justifies its best corrosion resistance.
3. The comparison of the present results with the previous of our systematic study evince not only the important influence of the sample geometry in the properties under study but also that the border effect, which causes the rings on the disk border, depends on the pressure, but not on temperature or time from the plasma nitriding process.

## 6. Acknowledgements

This work was partly supported by the Brazilian research funding agencies: Foundation for Research of the State of Minas Gerais (FAPEMIG) (APQ-02127-14 and APQ-02345-14), São Paulo Research Foundation (FAPESP), National Council for Scientific and Technological Development (CNPq) and Coordination for the Improvement of Higher Level -or Education- Personnel (CAPES). The authors also gratefully acknowledge the National Laboratory of Light Synchrotron (LNLS), Brazil Grants No. XDR1/9101 and XDR1/13458. The authors would like to thank Dr. L. M. Galego from IPEN (Brazil) for the helpful discussions.

## 7. References

1. De Las Heras E, Ybarra G, Lamas D, Cabo A, Dalibon EL, Brühl SP. Plasma nitriding of 316L stainless steel in two different $N_2$-$H_2$ atmospheres - Influence on microstructure and corrosion resistance. *Surface and Coatings Technology*. 2017;313:47-54.

2. Borgioli F, Galvanetto E, Bacci T. Low temperature nitriding of AISI 300 and 200 series austenitic stainless steels. *Vacuum*. 2016;127:51-60.

3. Yang WJ, Zhang M, Zhao YH, Shen ML, Lei H, Xu L, et al. Enhancement of mechanical property and corrosion resistance of 316 L stainless steels by low temperature arc plasma nitriding. *Surface and Coatings Technology*. 2016;298:64-72.

4. Borgioli F, Galvanetto E, Bacci T. Corrosion behaviour of low temperature nitrided nickel-free, AISI 200 and AISI 300 series austenitic stainless steels in NaCl solution. *Corrosion Science*. 2018;136:352-365.

5. Czerwiec T, Renevier N, Michel H. Low-temperature plasma-assisted nitriding. *Surface and Coatings Technology*. 2000;131(1-3):267-277.

6. Fewell MP, Mitchell DRG, Priest JM, Short KT, Collins GA. The nature of expanded austenite. *Surface and Coatings Technology*. 2000;131(1):300-306.

7. Singh V, Marchev K, Cooper CV, Meletis EI. Intensified plasma-assisted nitriding of AISI 316L stainless steel. *Surface and Coatings Technology*. 2002;160(2-3):249-258.

8. Fewell MP, Priest JM. High-order diffractometry of expanded austenite using synchrotron radiation. *Surface and Coatings Technology*. 2008;202(9):1802-1815.

9. Sun Y, Li XY, Bell T. X-ray diffraction characterisation of low temperature plasma nitrided austenitic stainless steels. *Journal of Materials Science*. 1999;34(19):4793-4802.

10. Tong K, Ye F, Che H, Lei MK, Miao S, Zhang C. High-density stacking faults in a supersaturated nitrided layer on austenitic stainless steel. *Journal of Applied Crystallography*. 2016;49(Pt 6):1967-1971.

11. Borgioli F, Fossati A, Galvanetto E, Bacci T. Glow-discharge nitriding of AISI 316L austenitic stainless steel: influence of treatment temperature. *Surface and Coatings Technology*. 2005;200(7):2474-2480.

12. Borgioli F, Fossati A, Galvanetto E, Bacci T, Pradelli G. Glow discharge nitriding of AISI 316L austenitic stainless steel: Influence of treatment pressure. *Surface and Coatings Technology*. 2006;200(18-19):5505-5513.

13. Olzon-Dionysio M, Olzon-Dionysio D, Campos M, Shigeyosi WT, Souza SD, de Souza S. Corrosion resistance of AISI 316L plasma nitrided at different temperatures and times. *Hyperfine Interactions*. 2019;240:26.

14. Campos M, de Souza SD, de Souza S, Olzon-Dionysio M. Improving the empirical model for plasma nitrided AISI 316L corrosion resistance based on Mössbauer spectroscopy. *Hyperfine Interactions*. 2011;203(1-3):105-112.

15. de Souza SD, Olzon-Dionysio M, Basso RLO, de Souza S. Mössbauer spectroscopy study on the corrosion resistance of plasma nitrided ASTM F138 stainless steel in chloride solution. *Materials Characterization*. 2010;61(10):992-999.

16. Olzon-Dionysio M, Campos M, Kapp M, de Souza S, de Souza SD. Influences of plasma nitriding edge effect on properties of 316 L stainless steel. *Surface and Coatings Technology*. 2010;204(21-22):3623-3628.

17. Franco AR Jr., Pintaúde G, Sinatora A, Pinedo CE, Tschiptschin AP. The use of a vickers indenter in depth sensing indentation for measuring elastic modulus and vickers hardness. *Materials Research*. 2004;7(3):483-491.

18. Campos M, de Souza SD, Martinez LG, Olzon-Dionysio M. Study of expanded austenite formed in plasma nitrided AISI 316L samples, using synchrotron radiation diffraction. *Materials Research*. 2014;17(5):1302-1308.

19. Picard S, Memet JB, Sabot R, Grosseau-Poussard JL, Rivière JP, Meilland R. Corrosion behaviour, microhardness and surface characterisation of low energy, high current ion implanted austenitic stainless steel. *Materials Science and Engineering: A*. 2001;303(1-2):163-172.

20. Öztürk O, Williamson DL. Phase and composition depth distribution analyses of low energy, high flux N implanted stainless steel. *Journal of Applied Physics*. 1995;77(8):3839-3850.

21. Saker A, Leroy C, Michel H, Frantz C. Properties of sputtered stainless steel-nitrogen coatings and structural analogy with low temperature plasma nitrided layers of austenitic steels. *Materials Science and Engineering: A*. 1991;140:702-708.

22. Campos M. *Investigação por espectroscopia Mössbauer das fases formadas e sua influência na resistência à corrosão do aço inoxidável austenítico AISI 316l nitretado*. [Dissertation]. São Carlos: Federal University of São Carlos; 2009.

23. Olzon-Dionysio M, Campos M, Higa OZ, da Cunha TF, de Souza SD. Investigating the correlation between some of the properties of plasma nitrided AISI 316L stainless steel. *Materials Research*. 2013;16(5):1052-1057.

24. Alves C Jr., da Silva EF, Martinelli AE. Effect of workpiece geometry on the uniformity of nitrided layers. *Surface and Coatings Technology*. 2001;139(1):1-5.

25. de Sousa RRM, de Araújo FO, Ribeiro KJB, Mendes MWD, da Costa JAP, Alves C Jr. Cathodic cage nitriding of samples with different dimensions. *Materials Science and Engineering: A*. 2007;465(1-2):223-227.

26. Hirota K, Takano Y, Yoshinaka M, Yamaguchi O. Hot Isostatic Pressing of Chromium Nitrides ($Cr_2N$ and CrN) Prepared by Self-Propagating High-Temperature Synthesis. *Journal of the American Ceramic Society*. 2001;84(9):2120-2122.

27. Aouadi SM, Schultze DM, Rohde SL, Wong KC, Mitchell KAR. Growth and characterization of $Cr_2N$/CrN multilayer coatings. *Surface and Coatings Technology*. 2001;140(3):269-277.

28. Dong H. S-phase surface engineering of Fe-Cr, Co-Cr and Ni-Cr alloys. *International Materials Reviews*. 2010;55(2):65-98.

29. Czerwiec T, He H, Weber S, Dong C, Michel H. On the occurrence of dual diffusion layers during plasma-assisted nitriding of austenitic stainless steel. *Surface and Coatings Technology*. 2006;200(18-19):5289-5295.

30. Wei R, Shogrin B, Wilbur PJ, Ozturk O, Williamson DL, Ivanov I, et al. The Effects of Low-Energy-Nitrogen-Ion Implantation on the Tribological and Microstructural Characteristics of AISI 304 Stainless Steel. *Journal of Tribolology*. 1994;116(4):870-876.

31. Pagitsas M, Sazou D. Current oscillations induced by chlorides during the passive-active transition of iron in a sulfuric acid solution. *Journal of Electroanalytical Chemistry*. 1991;471(2):132-145.

32. Jacobs H, Rechenbach D, Zachwieja U. Structure determination of γ′-$Fe_4N$ and ϵ-$Fe_3N$. *Journal of Alloys and Compounds*. 1995;227(1):10-17.

33. Leineweber A, Jacobs H, Hüning F, Lueken H, Kockelmann W. Nitrogen ordering and ferromagnetic properties of ϵ-$Fe_3N_{1+x}$ ($0.10 \leq x \leq 0.39$) and ϵ-$Fe_3(N_{0.80}C_{0.20})_{1.38}$. *Journal of Alloys and Compounds*. 2001;316(1-2):21-38.

34. Lv ZQ, Fu WT, Sun SH, Wang ZH, Fan W, Qv MG. Structural, electronic and magnetic properties of cementite-type $Fe_3X$ (X = B, C, N) by first-principles calculations. *Solid State Science*. 2010;12(3):404-408.

35. Schwarz U, Wosylus A, Wessel M, Dronskowski R, Hanfland M, Rau D, et al. High-Pressure-High-Temperature Behavior of ζ-$Fe_2N$ and Phase Transition to ϵ-$Fe_3N_{1.5}$. *European Journal of Inorganic Chemistry*. 2009;2009(12):1634-1639.

36. Henderson JK, Frederick GC. The occurrence and the crystal structure of α"-iron nitride; a new type of interstitial alloy formed during the tempering of nitrogen-martensite. *Proceedings of the Royal Society A. Mathematical, Physical and Engineering Sciences*. 1951;208(1093):19510155.

37 . Hasegawa M, Yagi T. Systematic study of formation and crystal structure of 3d-transition metal nitrides synthesized in a supercritical nitrogen fluid under 10 GPa and 1800 K using diamond anvil cell and YAG laser heating. *Journal of Alloys and Compounds*. 2005;403(1-2):131-142.

38. Lee TH, Kim SJ, Shin E, Takaki S. On the crystal structure of $Cr_2N$ precipitates in high-nitrogen austenitic stainless steel. III. Neutron diffraction study on the ordered $Cr_2N$ superstructure. *Acta Crystallographica B*. 2006;62(Pt 6):979-986.

39. Öztürk O, Okur S, Riviere JP. Structural and magnetic characterization of plasma ion nitrided layer on 316L stainless steel alloy. *Nuclear Instruments and Methods in Physics Research Section B: Beam Interactions with Materials and Atoms*. 2009;267(8-9):1540-1545.

40. Brink BK, Ståhl K, Christiansen TL, Frandsen C, Hansen MF, Somers MAJ. Composition-dependent variation of magnetic properties and interstitial ordering in homogeneous expanded austenite. *Acta Materialia*. 2016;106:32-39.